Wall stress enhanced exocytosis of extracellular vesicles as a possible mechanism of left-right symmetry-breaking in vertebrate development

Solowiej-Wedderburn, Josephine; Smith, David; Lopes, Susana; Montenegro-Johnson, Thomas

DOI:
10.1016/j.jtbi.2018.10.015

Wall stress enhanced exocytosis of extracellular vesicles as a possible mechanism of left-right symmetry-breaking in vertebrate development.

J. Solowiej-Wedderburn[a], D. J. Smith[b], S. S. Lopes[c], T. D. Montenegro-Johnson[b]

[a] *Dept of Mathematics, U. Surrey, Guildford, UK*
[b] *School of Mathematics, U. Birmingham, Birmingham, UK.*
[c] *1 NOVA Medical School Faculdade de Ciências Médicas, CEDOC, U. Nova de Lisboa, Lisboa, Portugal.*

Abstract

In certain vertebrate species, the developing embryo breaks left-right symmetry in a transient organising structure: the "Left-Right Organiser" (LRO) known as the "node" in mice, and "Kupffer's vesicle" in fish. Directional cilia-driven flow is integral to this symmetry-breaking process, however the mechanism by which this flow is translated into an asymmetric signal remains contested; the principal theories are either flow transport of vesicles containing morphogens, or flow mechanosensing by cilia. Whilst some recent work favours the morphogen theory, other findings seem to support mechanosensing. In this study, we consider a hypothesis whereby the cilia themselves drive the release of morphogen-carrying extracellular vesicles (EVs) into the LRO; namely, that fluid stresses on the cell membrane induce/enhance exocytosis of EVs. Using a mathematical model, we calculate significant wall normal and shear stresses for a range of typical cilium parameter values comparable to levels capable of enhancing exocytosis. This mechanism may be able to reconcile the apparently conflicting experimental evidence.

Keywords: Cilia-Driven Flow; Left-Right Symmetry-Breaking

1. Introduction

The organised left-right asymmetry of the vertebrate body plan (*situs solitus*) – the heart on the left and liver on the right in humans, for example – is a familiar feature of physiology. However, it has only relatively recently been discovered that a crucial part of this embryonic developmental process is a cilia-driven fluid flow occurring in the Left-Right Organiser (LRO), a transient structure also referred to as the "primitive node" in humans, "ventral node" in mice, "Kupffer's vesicle" (KV) in fish. The physical picture is that rotating "nodal" cilia, tilted towards an already-established body direction e.g. the posterior (Nonaka et al., 2005; Okada et al., 2005), drive a left-right asymmetric flow, which is necessary (Nonaka et al., 1998) and sufficient (Nonaka et al., 2002) to break symmetry. In particular, disruption of normal cilia motility can result in inversion of the body plan (*situs inversus*) or disorganised development (*heterotaxia*). In mouse, the LRO essentially comprises a 'carpet' of cilia on the ventral side of the embryo, tilted in the posterior direction, enclosed by an overlying membrane. In zebrafish, the LRO is an approximately spherical cavity with inward-pointing cilia on all sides, with a high density of cilia at the anterior end of the dorsal roof. These distinct morphologies produce qualitatively different flows (Fig. 1), though fulfil a similar developmental function - for a recent review of the fluid mechanics of the LRO, see Smith et al. (2019).

The conversion of this flow to asymmetric gene expression, and the subsequent body plan, is yet to be understood. Several key theories have been proposed and investigated:

1. Chemosensing: morphogens are distributed asymmetrically by flow, which then influence asymmetric signalling, gene expression and development. Two principal versions of this theory have been discussed:
   (i) Dissolved morphogen released from the nodal floor (Nonaka et al., 1998)
   (ii) Vesicle-enclosed morphogen transport (Tanaka et al., 2005; Cartwright et al., 2007)
2. Mechanosensing: cilia-driven flow exerts mechanical forces which are sensed asymmetrically. Most of the work on this theory has focused on calcium signalling by immotile cilia at the periphery of the node (McGrath et al., 2003).

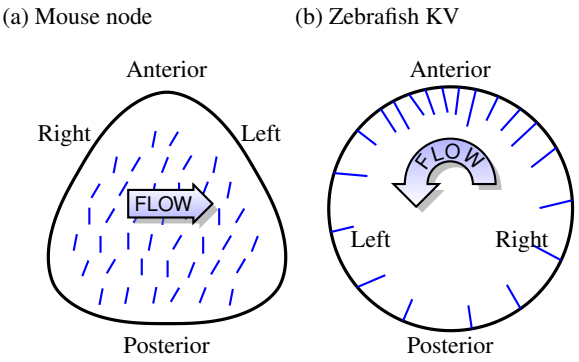

Figure 1: The arrangement of cilia, LRO geometry, and thus the resultant flow vary across species. (a) A schematic of the ventral node in mouse, showing cilia on the ventral surface, tilted towards the posterior, driving an average leftward flow above them. The standard experimental view of the node is from the ventral side, and hence Left and Right are transposed. (b) A schematic of the coronal midplane of the approximately spherical zebrafish KV (right). Cilia protrude from all sides, but are clustered in the anterior-dorsal region. For zebrafish KV, the standard experimental view is from the dorsal, rather than ventral side. Cilia drive an anticlockwise vortical flow that is stronger anterior corner, when the fluid is moving to the left.

Experimental and theoretical studies have provided significant information about the feasibility of each of these theories. For example, Cartwright et al. (2004) assessed the effect of advection-diffusion of dissolved morphogen in the enclosed cavity of the node, and suggested that a time-dependent inactivation process would be necessary to create an asymmetric gradient. Cartwright et al. also observed that very low Reynolds number flow is symmetric with regard to the magnitude of flow velocity and stress, and so mechanosensing would require a vectorial sensing capability.

Shinohara et al. (2012) made the remarkable finding that mutant mouse embryos expressing as few as two motile cilia were capable of consistent left-right symmetry-breaking. Their interpretation was that this lends more weight to a mechanical sensing mechanism in mouse. The flow produced by one or two motile cilia decays very rapidly in space; while mechanical forces are transmitted almost instantly, the timescale for morphogen or vesicle transport "from one side of the node to the other side" are extended greatly by the reduced flow field. To paraphrase: if vesicles are released over an extended area of a "two cilia node", relatively few will undergo significant leftward transport and hence the leftward-biasing effect will be minimal. Indeed whole-organ particle transport simulation (Smith et al., 2011) suggests that particle transport past the array of motile cilia is minimal. Sampaio et al. (2014) found that KV of zebrafish is much less robust to perturbations in cilia number. Associations between strong anterior flow velocity with normal development were found. It was suggested that these observations are more consistent with a mechanosensing theory.

However, a recent finding by Delling et al. (2016) cast major doubt on mechanosensing by presenting data that primary cilia in the node are in fact not capable of producing calcium signals in response to fluid flow; for further discussion of this issue, see Norris and Jackson (2016). Ferreira et al. (2017) used a combined experimental and theoretical approach in zebrafish embryos to explore several proposed flow sensing mechanisms; they argued that the number of immotile cilia in zebrafish KV is too small to achieve robust mechanosensing, due to the spatial variability of the flow field (although their observations of immotile cilia number are somewhat lower than the 20% reported by Tavares et al. (2017)). Instead, based on hydrodynamics and Brownian simulation, Ferreira et al. argued for chemosensing by cilia of membrane-bound extracellular vesicles (EVs) released preferentially in the anterior region, which was also suggested by Montenegro-Johnson et al. (2016). The process that might enable anterior release of vesicles would form an important part of this theoretical picture.

In this work, we will examine such a process, initially discussed by Okada et al. (2005),

> "Furthermore, cilia sweep just above the apical surface of the ciliated cell during their recovery stroke. This sweep might also facilitate the release of the putative morphogen bound to the lipid membrane or extracellular matrix."

In other words, the mechanical effect of cilia may be necessary to release extracellular vesicles carrying morphogens which are subsequently transported by the cilium beat – both mechanical and chemical cues are therefore necessary. While this idea appears to have received relatively little attention from theoreticians, recent evidence regarding the effect of shear stress on exocytosis (Jaé et al., 2015; Baratchi et al., 2016) motivates revisiting it. As we will see, the concept of localised stress-induced exocytosis may help to illuminate the feasibility of the anterior release theory in KV, and additionally explain the 'two cilium node' results of Shinohara et al. (2012). However, our main focus will be to estimate the fluid mechanical stresses exerted by tilted rotating cilia on the epithelial surface.

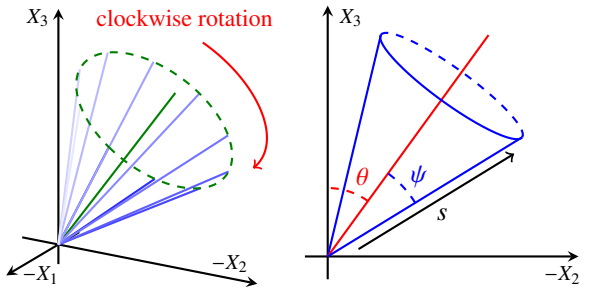

Figure 2: Schematic of the nodal cilium model. The cilium is modelled by a rigid rod beating in a conical envelope in a clockwise manner when viewed from tip to base; in order to best view this motion, the beat pattern is shown with negative X_1 and X_2 axes. The tilt angle θ, semi-cone and ψ and arclength s defining the beat are shown in the right panel.

2. Mathematical model

We consider the time-dependent flow driven by a single beating cilium. Nodal cilia are around 5 μm in length, and beat in a conical envelope. The frequency of this beating ranges between 10-40 Hz, and the semi-cone angle of the beat ranges between 30-60°, depending on the species. Thus, the Reynolds number for nodal flow is of the order $O(10^{-3}) \ll 1$, and the dynamics of nodal flow are well-modelled by the Stokes flow equations,

$$\mu\nabla^2\mathbf{u} - \nabla p + \mathbf{F} = \mathbf{0}, \quad \nabla\cdot\mathbf{u} = 0, \tag{1}$$

for $\mathbf{u}$ the flow velocity, p the pressure in the fluid, μ the fluid viscosity, and $\mathbf{F}$ body forces acting on the flow.

Following the methodology of Smith et al. (2008), we will approximate the kinematics of the cilium by a rigid rod, of fixed length L, rotating about an axis so as to trace out the envelope of a cone tilted in the negative X_2-direction, yielding the centreline $\mathbf{X}(s,t)$,

$$X_1(s,t) = \quad s\sin\psi\cos\omega t, \tag{2a}$$
$$X_2(s,t) = -s\sin\psi\sin\omega t\cos\theta - s\cos\psi\sin\theta, \tag{2b}$$
$$X_3(s,t) = -s\sin\psi\sin\omega t\sin\theta + s\cos\psi\cos\theta, \tag{2c}$$

with velocity

$$\dot{X}_1(s,t) = -s\omega\sin\psi\sin\omega t, \tag{3a}$$
$$\dot{X}_2(s,t) = -s\omega\sin\psi\cos\omega t\cos\theta \tag{3b}$$
$$\dot{X}_3(s,t) = -s\omega\sin\psi\cos\omega t\sin\theta \tag{3c}$$

for $s \in [0, L]$ the arclength along the rod, ψ the semi-cone angle and θ the tilt angle, as shown in figure 2. As in Smith et al. (2008), we approximate the force per unit length that the cilium exerts upon the fluid via the local drag approximation of resistive force theory (Gray and Hancock, 1955; Lighthill, 1976). Noting that, for this simplified model, the motion of the cilium through the fluid is always perpendicular to its centreline, the force that the cilium exerts on the fluid may be approximated

$$\mathbf{F}(s,t) = C_\perp\dot{\mathbf{X}}(s,t), \quad C_\perp = \frac{8\pi\mu}{1+2\log(2q/a)}, \tag{4}$$

for q an intermediate length scale of the order $O(\sqrt{aL})$, so that $a \ll q \ll L$ for a the cilium radius (Gueron and Liron, 1992). Following Smith et al. (2008) we use the values $q = 0.6$ μm and $a = 0.1$ μm, noting that the precise value of these parameters only has a small effect on $C_\perp$, which is given by $C_\perp = 1.34\pi\mu$ in what follows.

The flow driven by the cilium at any instant may then be coarsely approximated by a line distribution of point forces representing the cilium, over an infinite no-slip plane boundary at $x_3 = 0$. The flow velocity at a point $\mathbf{x}$ in the fluid arising from a point force of strength $\mathbf{f}$ located at $\mathbf{y}$ over a plane boundary is given by $u_i(\mathbf{x}) = B_{ij}(\mathbf{x},\mathbf{y})f_j$, for Blakelet tensor (Blake, 1971)

$$B_{ij} = \frac{1}{8\pi\mu}\Bigg[\left(\frac{\delta_{ij}}{r} + \frac{r_i r_j}{r^3}\right) - \left(\frac{\delta_{ij}}{R} + \frac{R_i R_j}{R^3}\right) + 2y_3\left(\delta_{j\alpha}\delta_{\alpha l} - \delta_{j3}\delta_{3l}\right)\frac{\partial}{\partial R_l}\left(\frac{y_3 R_i}{R^3} - \left(\frac{\delta_{i3}}{R} + \frac{R_i R_3}{R^3}\right)\right)\Bigg], \tag{5}$$

with δ_{ij} the Kronecker delta, $r_i = x_i - y_i$, $r = |\mathbf{r}|$, and $R_{1,2} = x_{1,2} - y_{1,2}$, $R_3 = x_3 + y_3$, with $R = |\mathbf{R}|$. The indices $i, j = 1, 2, 3$, whereas $\alpha = 1, 2$, with summation convention applied when indices are repeated. Thus, the flow generated by a whirling cilium may be approximated by a simple integral of known quantities

$$u_i(\mathbf{x},t) = \int_0^L B_{ij}(\mathbf{x},\mathbf{X}(s,t))C_\perp\dot{X}_j(s,t)\,\mathrm{d}s. \tag{6}$$

To calculate wall stresses, we require the partial derivatives of the flow generated by the cilium, which may be found by taking the derivative of equation (6) with respect to the evaluation point $\mathbf{x}$. Bringing the derivative into the integral

$$\frac{\partial\left(u_i(\mathbf{x})\right)}{\partial x_k} = \int_0^L \frac{\partial}{\partial x_k}\Big(B_{ij}(\mathbf{x},\mathbf{X}(s,t))\Big)C_\perp\dot{X}_j(s,t)\,\mathrm{d}s, \tag{7}$$

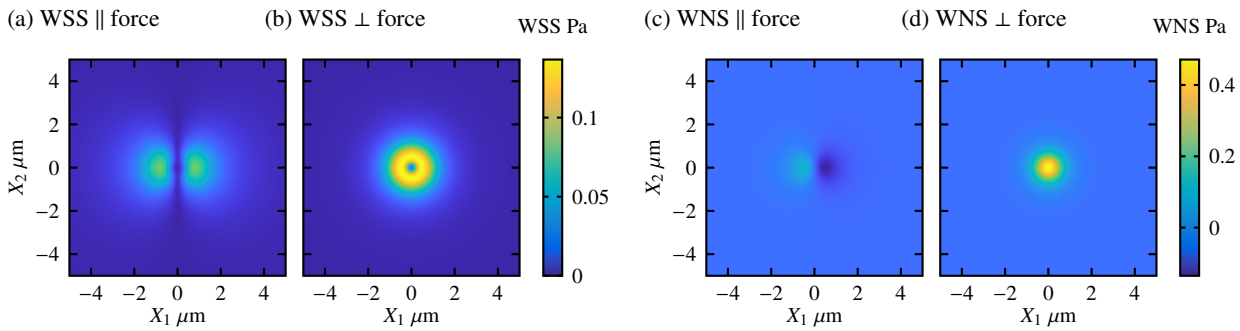

Figure 3: Plots of the flow WSS and WNS induced by a point force of 1 pN located at $(0, 0, 1)$ μm above the plane boundary, when the force is directed both parallel and perpendicular to the wall. (a) WSS for $\mathbf{F} = (1, 0, 0)$ pN, and (b) WSS for $\mathbf{F} = (0, 0, 1)$ pN. (c) WNS for $\mathbf{F} = (1, 0, 0)$ pN, and (d) WNS for $\mathbf{F} = (0, 0, 1)$ pN. Note that, when the magnitude of the force is specified, this result is independent of the fluid viscosity.

where we find the derivative of the Blakelet to be,

$$\begin{aligned}\frac{\partial B_{ij}}{\partial x_k} = \frac{1}{8\pi\mu}\Bigg[&\left(-\frac{r_k\delta_{ij}}{r^3} + \frac{r_j\delta_{ik}}{r^3} + \frac{r_i\delta_{jk}}{r^3} - \frac{3r_ir_jr_k}{r^5}\right)\\ &-\left(-\frac{R_k\delta_{ij}}{R^3} + \frac{R_j\delta_{ik}}{R^3} + \frac{R_i\delta_{jk}}{R^3} - \frac{3R_iR_jR_k}{R^5}\right)\\ &+ 2y_3(\delta_{j\alpha}\delta_{\alpha l} - \delta_{j3}\delta_{3l})\frac{\partial}{\partial R_l}\Bigg(\frac{y_3\delta_{ik}}{R^3} - \frac{3R_iR_ky_3}{R^5}\\ &+ \frac{R_k\delta_{i3}}{R^3} - \frac{R_3\delta_{ik}}{R^3} - \frac{R_i\delta_{k3}}{R^3} + \frac{3R_iR_kR_3}{R^5}\Bigg)\Bigg].\end{aligned} \tag{8}$$

A fully-expanded version of this derivative for simpler calculation is given in the appendix.

Since the WSS will depend upon flow derivatives evaluated on the no-slip wall, we note $\partial u_i/\partial x_k = 0$ for $i = 1, 2, 3$, $k = 1, 2$. Furthermore, when $i = 3 = k$, on the plane $x_3 = 0$, $r = R$, $r_1 = R_1$, $r_2 = R_2$ and $r_3 = y_3 = -R_3$, and substituting into the Blakelet derivative it is possible to show that $\partial B_{3j}/\partial x_3 = 0$, and hence $\partial u_3/\partial x_3 = 0$. As such, only the terms $\partial u_1/\partial x_3$ and $\partial u_2/\partial x_3$ will contribute to the WSS.

To evaluate the WSS, we note that the stress tensor is given by,

$$\sigma_{ij} = -p\delta_{ij} + \mu\left(\frac{\partial u_i}{\partial x_j} + \frac{\partial u_j}{\partial x_i}\right), \tag{9}$$

so that the traction on the plane boundary $x_3 = 0$ is $\sigma_{ij}n_j$, with $\mathbf{n} = [0, 0, 1]^T$. The WNS is then the normal component of the traction,

$$\tau_n = n_i\sigma_{ij}n_j = \sigma_{33} = -p, \tag{10}$$

so that the WSS is the traction, minus the WNS vector,

$$\tau_i = \sigma_{ij}n_j - n_k\sigma_{kj}n_jn_i. \tag{11}$$

Using the above simplifications, this vector reduces to

$$\tau_i = \mu[\partial u_1/\partial x_3, \partial u_2/\partial x_3, 0]^T, \tag{12}$$

so that finally, the magnitude of the WSS on the boundary from a collection of point forces is given by

$$\tau = \mu\sqrt{\left(\frac{\partial u_1}{\partial x_3}\right)^2 + \left(\frac{\partial u_2}{\partial x_3}\right)^2}. \tag{13}$$

Whilst there is experimental evidence for a possible role of WSS in enhancing exocytosis, perhaps by stretching the cell membrane, WNS may also play a role by "pulling out" EVs from the membrane. The pressure (ie WNS) relative to hydrostatic pressure is given by the pressure-Blakelet (Blake, 1971),

$$p_i = \frac{1}{4\pi}\left[\frac{r_i}{r^3} - \frac{R_i}{R^3} - 2y_3(\delta_{i\alpha}\delta_{\alpha l} - \delta_{i3}\delta_{3l})\frac{\partial}{\partial R_l}\left(\frac{R_3}{R^3}\right)\right]. \tag{14}$$

Thus, the additional WNS jump across the membrane due to the cilium-driven flow is given by,

$$-p(\mathbf{x}, t) = -\int_0^L p_i(\mathbf{x}, \mathbf{X}(s, t))C_\perp\dot{X}_i(s, t)\,\mathrm{d}s, \tag{15}$$

for $x_3 = 0$. We now proceed to calculate these stresses for our model cilium.

3. Results

We begin our analysis by considering the stresses on the plane boundary $x_3 = 0$ induced by a point force of 1 pN at $\mathbf{y} = (0, 0, h)$, where $h = 1$ μm. For a force parallel to the wall, the WSS is shown in Fig. 4a, with the perpendicular force WSS shown in Fig. 4b. The WNS for parallel (Fig. 4c) and perpendicular (Fig. 4d) forces

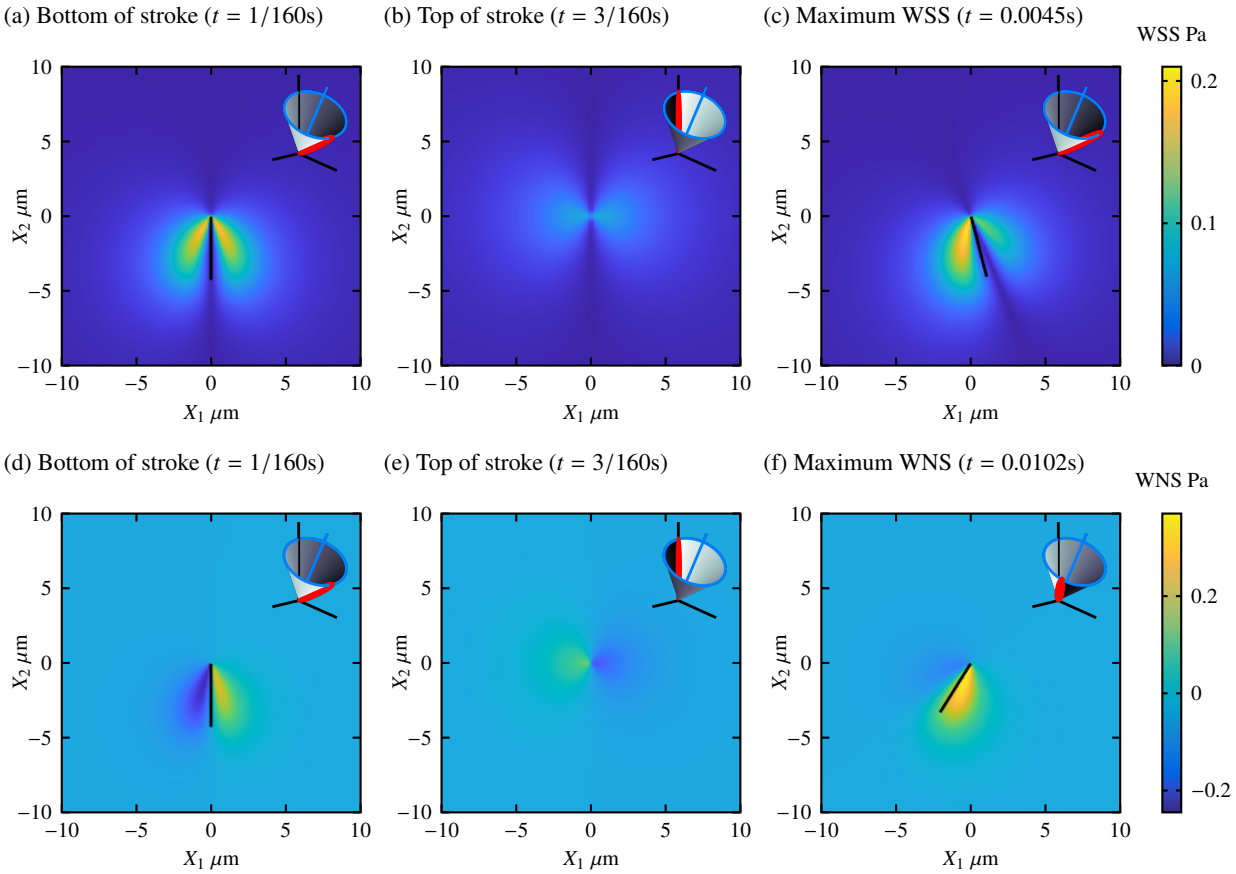

Figure 4: WSS and WNS on the cell membrane during the cilium stroke, with parameters: cilium length 5 μm, $\omega = 80\pi$ rad/s corresponding to a frequency of 40 Hz, $\theta = 30°$, $\psi = 30°$ and $\mu = 10^{-3}$ Pa·s. (a) WSS at the bottom of the stroke, showing zero WSS directly under the cilium. The WNS at the same instant (d) shows negative WNS (pushing on the membrane) ahead of the cilium, and positive WNS following (pulling-out from the membrane). At the top of the stroke, WSS (b) and WNS (e) are considerably lower. The maximum WSS stress (c) occurs just before the bottom of the stroke, in the same region of the cell membrane as the maximum positive WNS (f) moments later, motivating the theory of a combined role.

is also shown, and we note that a positive WNS corresponds to a region of low pressure above the boundary, yielding an "upwards" force.

The plots of WSS reveal two perhaps unexpected features; it is reasonable to expect, at least for the parallel point force, that the maximum WSS induced would be directly under the force i.e., the shortest distance between the wall and the force driving the flow. In fact, the WSS is zero directly under both parallel and perpendicular forces and thus, by linearity, under a force of any direction. The second, more complex, feature is that for a parallel force, the wall shear stress is zero on a line passing directly under the force in a perpendicular direction. We now explain this behaviour.

Without loss of generality we consider a single point force oriented parallel to the boundary, $f = [1, 0, 0]^T$. Then

$$\frac{\partial u_1}{\partial x_3} = \frac{\partial B_{11}}{\partial x_3} f_1, \quad \frac{\partial u_2}{\partial x_3} = \frac{\partial B_{21}}{\partial x_3} f_1. \tag{16}$$

Substitution of the line $\mathbf{x} = (0, b, 0)$ for $b \in \mathbb{R}$ into the Blakelet derivative gives

$$\frac{\partial B_{11}}{\partial x_3} = \frac{h\delta_{11}}{r^3} + \frac{h\delta_{11}}{R^3} + 2h\left(-\frac{\delta_{33}\delta_{11}}{R^3}\right) = 0, \tag{17}$$

since $r = \sqrt{b^2 + h^2} = R$. All components of $\partial B_{21}/\partial x_3$ are zero, giving the zero WSS result. Note that, along this line, it is the contribution from the higher-order image singularities that cancels the contribution from the two stokeslets.

It is possible to gain further physical insight by evaluating the flow a small distance ϵz above the boundary.

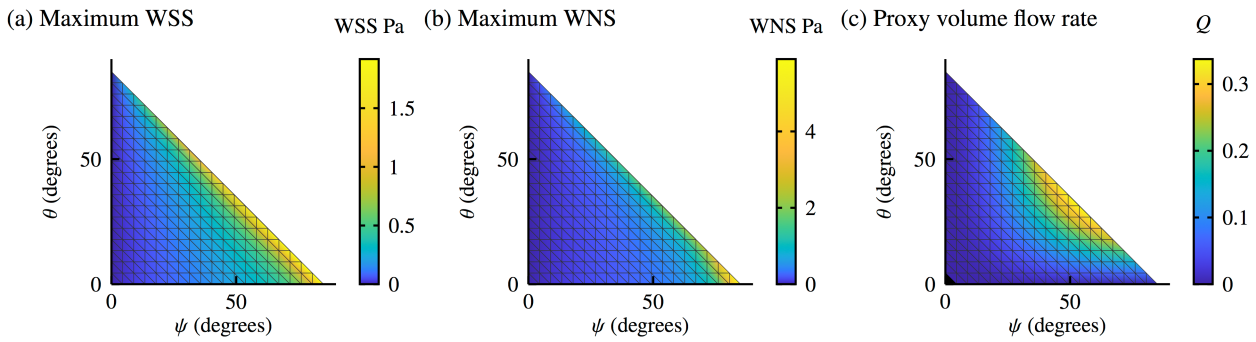

Figure 5: The effects of varying tilt and semi-cone angles on important quantities of nodal flow, for cilium length 5 μm, beat frequency 40 Hz, and fluid viscosity $\mu = 10^{-3}$ Pa·s. (a) The maximum WSS during a beat, and (b) the maximum WSS during a beat, both showing maxima at $\theta = 0°, \psi = 85°$. (c) A scaled, dimensionless, proxy for the directional volume flow rate arising from a beating nodal cilium, with maximum at $\theta = 31°, \psi = 54°$.

Then we have

$$x_1 = 0, \quad x_2 = b, \quad x_3 = \epsilon z, \tag{18a}$$
$$X_1 = 0, \quad X_2 = 0, \quad X_3 = h, \tag{18b}$$

and thus

$$r_1 = 0, \quad r_2 = b, \quad r_3 = \epsilon z - h, \tag{19a}$$
$$R_1 = 0, \quad R_2 = b, \quad R_3 = \epsilon z + h \tag{19b}$$

and u_1 is given by $u_1 = B_{11} f_1$. After some work, we find that

$$u_1(z) = \frac{6\epsilon^2 z^2 h^2}{8\pi\mu(b^2 + h^2)^{5/2}} + O(\epsilon^3). \tag{20}$$

We thus see that close to the boundary, the flow along this line depends quadratically on z, rather than as a simple shear flow, and as such the derivative evaluated at the boundary is equal to zero.

As a consequence of this behaviour, when the cilium is at the lowest point of its stroke, the WSS directly under the cilium is zero, not at its maximum as one might intuitively expect. This result depends on two assumptions, that the cilium is a rigid, straight rod, and that the force per unit length it exerts on the fluid is parallel to its direction of motion. In practice, nodal cilia more than 5 microns in length begin to develop helicity to their beat (Pintado et al., 2017), likely due to an increase in the ratio of viscous to elastic forces (Qian et al., 2008), known as the "Machin" (Machin, 1958) or equivalently "Sperm" number (Lowe, 2003) of the fluid-structure interaction, and non-local hydrodynamic interactions may result in some non-perpendicular force components. However it is likely that for the majority of nodal cilia, these effects will be small, and so we still expect maxima of WSS in front and behind of the beating cilium.

For a "typical" cilium, 5 μm in length, with $\theta = \psi = 30°$, beating at 40 Hz in a fluid with viscosity $\mu \approx 10^{-3}$ Pa·s, the maximum WSS occurs when the cilium is just either side of the lowest part of the beat, and is 0.21 Pa. The distribution of WSS and WNS is shown at 3 instances of the beat in figure 4. Additionally, we note that the maximal magnitude of WNS is somewhat higher, at 0.37 Pa. The WNS is negative in front of the cilium, representing fluid pushing against the boundary, and positive behind. In particular, we note that the maximum in WSS occurs in a similar location to the maximum in WNS, only slightly earlier in the beat (Fig. 4c,f), so that the negative pressure following the cilium might serve to further enhance exocytosis by "pulling out" EVs from the cell membrane: a potentially complementary mechanism to the membrane stretching induced by WSS.

By increasing the tilt or semi-cone angles, it is possible to increase the maximum wall stresses. Figure 5a,b shows the maximum WSS and WNS respectively achieved during the beat (at 40 Hz) of a 5 μm cilium in a fluid with viscosity $\mu \approx 10^{-3}$ Pa as a function of tilt θ and semi-cone angle ψ. The data have been calculated in the region such that $\theta + \psi \leq 85°$, so that the cilium does not contact the plane boundary. We note that very high values of WSS and WNS may be obtained for large semi-cone angle; increasing the semi-cone angle both increases the speed of the cilium tip, and brings the cilium closer to the plane boundary, both of which enhance wall stresses. However, we note that a) cilia with larger semi-cone angles may beat at a lower frequency due to power limitations, reducing these values, and b) 40 Hz is appropriate for some zebrafish nodal cilia, but the beat frequency may be somewhat lower (10-20 Hz) in mouse - by linearity of Stokes flow, the

wall stress is is proportional to the frequency, so that the precise values will vary between species. Finally, it is important to note that nodal cilia do not simply maximise wall stress; they must also drive a leftward flow. Figure 5c shows $Q = \sin^2\psi \sin\theta$, a dimensionless proxy for the volume flow rate arising from a nodal cilium (Smith et al., 2008), as a function of θ and ψ. The optimal volume flow rate occurs approximately when $\theta = 31°$ and $\psi = 54°$, for which the maximum WSS is 1.6 Pa and WNS is 2 Pa.

This places an "optimum" WSS and WNS slightly in excess of the 1 Pa (reported as 10 dyn/cm^2) found by Baratchi et al. (2016) to enhance exocytosis in human vascular endothelial cells. This value is likely an upper-bound on the value in the mouse node; a high beat frequency was used, we have chosen a beat pattern that approaches close to the surface, and nodal cilia beat slightly more slowly in the portion of their beat close to the wall. However, even after taking this into account cilia still produce significant wall stresses. Furthermore, there are unknown differences in nodal cell mechanical properties vs human vascular endothelial cells, such as stiffness, and furthermore that the viscosity of the nodal fluid is likely slightly higher than that of pure water, which would increase the value of WSS. We thus believe that the range of our calculated values of WSS, together with the potential complementary mechanism from WNS, are close enough to the significant 1 Pa result of Baratchi et al. (2016) to motivate experimental investigation.

4. Discussion

In this study, we carried out a quantitative investigation inspired by Okada et al.'s idea (Okada et al., 2005) that cilia-induced viscous stresses may assist with releasing morphogen via EVs, calculating the WSS and WNS induced by a beating nodal cilium as it passes across the cell surface. We estimated a range of values for WSS and WNS comparable to 1 Pa, based on a 40 Hz beat frequency and 5 μm cilium, and theorised that this may be sufficient to enhance exocytosis of EVs. In view of the observation that a WSS of 1 Pa significantly enhances exocytosis of TRPV4 channels in human vascular endothelial cells (Baratchi et al., 2016), the values we have calculated suggest that cilia-induced exocytosis is not an unreasonable hypothesis and therefore warrants further investigation.

Whilst it is known that left-right directional flow in the LRO is critical for breaking the symmetry of the left-right body axis of some vertebrates, the process by

(a) Two-cilium mouse node (b) Zebrafish KV

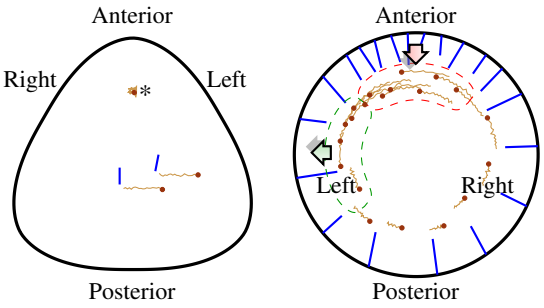

Figure 6: A cilia-induced EV release explanation for conflicting experimental data. (a) A schematic of EV transport in two-cilium mouse mutants, with EVs released by cilia-driven fluid stresses entering the node in the perfect location to travel leftwards. In contrast, particles released away from the cilia would be dominated by Brownian motion, as with the particle marked *. (b) A mechanistic schematic of cilium-induced EV release in zebrafish. Each particle is shown starting at a random position above its corresponding cilium tip. It is then advected anticlockwise by a vortical flow that is faster in the anterior half. After some time, EVs are reabsorbed, resulting in a left-right asymmetric signal. The hatched areas approximate (top) the area of increased particle release, and (left) the area of increased absorption.

which this flow is coupled to left-right asymmetric development has remained contested for over 10 years. As outlined in the introduction, the mechanical sensing role of cilia is disputed, however there are aspects of the chemosensory/extracellular vesicle theory that require further explanation.

- In mouse, specifically mutants with few (2–6) cilia, how is a significantly biased morphogen distribution produced from a spatially-restricted flow (Shinohara et al., 2012)?

- In KV, how are morphogen parcels released to ensure they reach the left before the right (Montenegro-Johnson et al., 2016; Ferreira et al., 2017)? Further, why is strong anterior flow apparently necessary for left-right symmetry breaking (Sampaio et al., 2014)?

The concept of cilia-induced EV release provides a potential answer (Fig. 6). In respect of mouse mutants with very few cilia, if EVs are only released in the vicinity of motile cilia, their distribution will be consistently biased to the left – even if their transport is limited (Fig. 6a). In respect of zebrafish Kupffer's vesicle, the strong anterior flow produced by dense anterior ciliation will induce greater exocytosis in the anterior region. As discussed by Montenegro-Johnson et al. (2016) and Ferreira et al. (2017), EVs released at the anterior are ini-

tially transported to the left, and hence the left side receives a stronger EV signal (Fig. 6b).

Moving forward, it may be important to consider detailed mechanical descriptions of the cilium and cell in models of left-right symmetry-breaking. Nodal cilia are connected via a basal body to the apical actin cytoskeleton (Kim and Dynlacht, 2013), which is known to sense and respond to tension from beating cilia in multiciliated ependymal cells in brain cavities (Mahuzier et al., 2018). In addition to stresses in the cytoskeleton, cilium beating may also produce further stresses in the membrane, or even cause the surface of the membrane to deform. Such modelling would require both detailed modelling of the doublet microtubule internal structure of the cilia, as well as experimental characterisation of material properties of the basal connection, cell membrane, and apical actin cytoskeleton. Future modelling will also need to couple time-dependent flow models of the LRO (Smith et al., 2008; Sampaio et al., 2014), which incorporate advection-diffusion of particles, with time-dependent influx conditions dependent on membrane stresses.

However whilst the current work is theoretical in nature, we hope that the manner in which the theory of cilia-induced local vesicle release reconciles diverse recent data will provide a catalyst for further experimental study of the system, leading to an integrative mechanochemical understanding of left-right symmetry breaking.

Acknowledgements

JSW acknowledges a studentship from EPSRC training grant EP/N509772/1. SSL would like to acknowledge Fundação para a Ciência e a Tecnologia grant: PTDC/BEX-BID/1411/2014 and IF/00951/2012. DJS acknowledges EPSRC Healthcare Technologies Challenge Award EP/N021096/1. TDMJ acknowledges support from a Royal Commission for the Exhibition of 1851 Research Fellowship, and EPSRC grant EP/R041555/1.

Appendix A. The Blakelet Derivative

To differentiate the Blakelet, we split it into three terms: the Stokeslet, and its image,

$$\left(\frac{\delta_{ij}}{r}+\frac{r_i r_j}{r^3}\right), \qquad \left(\frac{\delta_{ij}}{R}+\frac{R_i R_j}{R^3}\right), \tag{A.1}$$

and a third combined term comprising the 'stokes doublet' and a 'source-doublet' images, given by

$$2y_3\left(\delta_{j\alpha}\delta_{\alpha l}-\delta_{j3}\delta_{3l}\right)\frac{\partial}{\partial R_l}\left(\frac{y_3 R_i}{R^3}-\left(\frac{\delta_{i3}}{R}+\frac{R_i R_3}{R^3}\right)\right), \tag{A.2}$$

where the tensor $\delta_{j\alpha}\delta_{\alpha l}-\delta_{j3}\delta_{3l}$ is $+1$ when $j=l=1,2$ and -1 when $j=l=3$. To differentiate the stokeslet, note $\partial r/\partial x_k = r_k/r$, and $\partial r_i/\partial x_k = \delta_{ik}$, so that the first term in (A.1) gives,

$$\left(-\frac{r_k\delta_{ij}}{r^3}+\frac{r_j\delta_{ik}}{r^3}+\frac{r_i\delta_{jk}}{r^3}-\frac{3r_i r_j r_k}{r^5}\right), \tag{A.3}$$

and we can differentiate the second term in (A.1) in a similar manner. Equation (A.2) gives

$$\begin{aligned}
&\frac{\partial}{\partial x_k}\left(2y_3\left(\delta_{j\alpha}\delta_{\alpha l}-\delta_{j3}\delta_{3l}\right)\frac{\partial}{\partial R_l}\left(\frac{y_3R_i}{R^3}-\left(\frac{\delta_{i3}}{R}+\frac{R_iR_3}{R^3}\right)\right)\right)\\
&=2y_3\left(\delta_{j\alpha}\delta_{\alpha l}-\delta_{j3}\delta_{3l}\right)\frac{\partial}{\partial R_l}\left(\frac{\partial}{\partial x_k}\left(\frac{y_3R_i}{R^3}-\left(\frac{\delta_{i3}}{R}+\frac{R_iR_3}{R^3}\right)\right)\right)\\
&=2y_3(\delta_{j\alpha}\delta_{\alpha l}-\delta_{j3}\delta_{3l})\frac{\partial}{\partial R_l}\Big(\frac{y_3\delta_{ik}}{R^3}-\frac{3R_iR_ky_3}{R^5}\\
&\qquad+\frac{R_k\delta_{i3}}{R^3}-\frac{R_3\delta_{ik}}{R^3}-\frac{R_i\delta_{k3}}{R^3}+\frac{3R_iR_kR_3}{R^5}\Big).
\end{aligned} \tag{A.4}$$

In this way, equation (8) can be obtained. To give the derivative explicitly, in a form suitable for calculation, we also need to expand the partial derivative with respect to R_l. Expanding the derivative in (A.4), and noting that $\delta_{j\alpha}\delta_{\alpha l}-\delta_{j3}\delta_{3l}=\delta_{j1}\delta_{1l}+\delta_{j2}\delta_{2l}-\delta_{j3}\delta_{3l}$, we sum over the repeated index l, and using $R_3-y_3=x_3$ we obtain,

$$\begin{aligned}
\frac{\partial B_{ij}}{\partial x_k}=\frac{1}{8\pi\mu}\Big[&\left(-\frac{r_k\delta_{ij}}{r^3}+\frac{r_j\delta_{ik}}{r^3}+\frac{r_i\delta_{jk}}{r^3}-\frac{3r_ir_jr_k}{r^5}\right)\\
&-\left(-\frac{R_k\delta_{ij}}{R^3}+\frac{R_j\delta_{ik}}{R^3}+\frac{R_i\delta_{jk}}{R^3}-\frac{3R_iR_jR_k}{R^5}\right)\\
&+2y_3\Big(\delta_{j1}\Big(-\frac{\delta_{k3}\delta_{i1}}{R^3}+\frac{3R_kx_3\delta_{i1}}{R^5}+\frac{\delta_{k1}\delta_{i3}}{R^3}-\frac{3R_kR_1\delta_{i3}}{R^5}\\
&+\frac{3}{R^5}(R_ix_3\delta_{k1}+R_1x_3\delta_{ik}+R_1R_i\delta_{k3})-\frac{15R_1R_iR_kx_3}{R^7}\Big)\\
&+\delta_{j2}\Big(-\frac{\delta_{k3}\delta_{i2}}{R^3}+\frac{3R_kx_3\delta_{i2}}{R^5}+\frac{\delta_{k2}\delta_{i3}}{R^3}-\frac{3R_kR_2\delta_{i3}}{R^5}\\
&+\frac{3}{R^5}(R_ix_3\delta_{k2}+R_2x_3\delta_{ik}+R_2R_i\delta_{k3})-\frac{15R_2R_iR_kx_3}{R^7}\Big)\\
&+\delta_{j3}\Big(\frac{3R_ky_3\delta_{i3}}{R^5}+\frac{\delta_{ik}}{R^3}-\frac{3R_kR_i}{R^5}\\
&-\frac{3}{R^5}(R_ix_3\delta_{k1}+R_3x_3\delta_{ik}+R_3R_i\delta_{k3})+\frac{15R_3R_iR_kx_3}{R^7}\Big)\Big)\Big],
\end{aligned} \tag{A.5}$$

in a form ready for evaluation. This form of the Blakelet derivative was verified via central finite differences of the Blakelet tensor.

References

Baratchi, S., Almazi, J., Darby, W., Tovar-Lopez, F., Mitchell, A., McIntyre, P., 2016. Shear stress mediates exocytosis of functional TRPV4 channels in endothelial cells. Cellular and Molecular Life Sciences 73 (3), 649–666.

Blake, J., 1971. A note on the image system for a stokeslet in a no-slip boundary. In: Mathematical Proceedings of the Cambridge Philosophical Society. Vol. 70. Cambridge University Press, pp. 303–310.

Cartwright, J., Piro, O., Tuval, I., 2004. Fluid-dynamical basis of the embryonic development of left-right asymmetry in vertebrates. Proceedings of the National Academy of Sciences of the United States of America 101 (19), 7234–7239.

Cartwright, J. H., Piro, N., Piro, O., Tuval, I., 2007. Embryonic nodal flow and the dynamics of nodal vesicular parcels. Journal of The Royal Society Interface 4 (12), 49–56.

Delling, M., Indzhykulian, A., Liu, X., Li, Y., Xie, T., Corey, D., Clapham, D., 2016. Primary cilia are not calcium-responsive mechanosensors. Nature 531 (7596), 656.

Ferreira, R. R., Vilfan, A., Jülicher, F., Supatto, W., Vermot, J., 2017. Physical limits of flow sensing in the left-right organizer. eLife 6.

Gray, J., Hancock, G. J., 1955. The propulsion of sea-urchin spermatozoa. J. Exp. Biol. 32, 802–814.

Gueron, S., Liron, N., 1992. Ciliary motion modeling, and dynamic multicilia interactions. Biophysical Journal 63 (4), 1045–1058.

Jaé, N., McEwan, D., Manavski, Y., Boon, R., Dimmeler, S., 2015. Rab7a and Rab27b control secretion of endothelial microRNA through extracellular vesicles. FEBS letters 589 (20PartB), 3182–3188.

Kim, S., Dynlacht, B. D., 2013. Assembling a primary cilium. Current opinion in cell biology 25 (4), 506–511.

Lighthill, J., 1976. Flagellar hydrodynamics. SIAM review 18 (2), 161–230.

Lowe, C. P., 2003. Dynamics of filaments: modelling the dynamics of driven microfilaments. Philosophical Transactions of the Royal Society of London B: Biological Sciences 358 (1437), 1543–1550.

Machin, K. E., 1958. Wave propagation along flagella. J. Exp. Biol. 35 (4), 796–806.

Mahuzier, A., Shihavuddin, A., Fournier, C., Lansade, P., Faucourt, M., Menezes, N., Meunier, A., Garfa-Traoré, M., Carlier, M.-F., Voituriez, R., et al., 2018. Ependymal cilia beating induces an actin network to protect centrioles against shear stress. Nature communications 9 (1), 2279.

McGrath, J., Somlo, S., Makova, S., Tian, X., Brueckner, M., 2003. Two populations of node monocilia initiate left-right asymmetry in the mouse. Cell 114 (1), 61–73.

Montenegro-Johnson, T., Baker, D., Smith, D., Lopes, S., 2016. Three-dimensional flow in Kupffer's vesicle. Journal of Mathematical Biology 73 (3), 705–725.

Nonaka, S., Shiratori, H., Saijoh, Y., Hamada, H., 2002. Determination of left–right patterning of the mouse embryo by artificial nodal flow. Nature 418 (6893), 96.

Nonaka, S., Tanaka, Y., Okada, Y., Takeda, S., Harada, A., Kanai, Y., Kido, M., Hirokawa, N., 1998. Randomization of left–right asymmetry due to loss of nodal cilia generating leftward flow of extraembryonic fluid in mice lacking KIF3B motor protein. Cell 95 (6), 829–837.

Nonaka, S., Yoshiba, S., Watanabe, D., Ikeuchi, S., Goto, T., Marshall, W. F., Hamada, H., 2005. De novo formation of left–right asymmetry by posterior tilt of nodal cilia. PLoS Biology 3 (8), e268.

Norris, D., Jackson, P., 2016. Cell biology: Calcium contradictions in cilia. Nature 531 (7596), 582.

Okada, Y., Takeda, S., Tanaka, Y., Belmonte, J.-C. I., Hirokawa, N., 2005. Mechanism of nodal flow: a conserved symmetry breaking event in left-right axis determination. Cell 121 (4), 633–644.

Pintado, P., Sampaio, P., Tavares, B., Montenegro-Johnson, T., Smith, D., Lopes, S., 2017. Dynamics of cilia length in left–right development. Royal Society Open Science 4 (3), 161102.

Qian, B., Powers, T. R., Breuer, K. S., 2008. Shape transition and propulsive force of an elastic rod rotating in a viscous fluid. Physical review letters 100 (7), 078101.

Sampaio, P., Ferreira, R. R., Guerrero, A., Pintado, P., Tavares, B., Amaro, J., Smith, A. A., Montenegro-Johnson, T., Smith, D. J., Lopes, S. S., 2014. Left-right organizer flow dynamics: how much cilia activity reliably yields laterality? Developmental cell 29 (6), 716–728.

Shinohara, K., Kawasumi, A., Takamatsu, A., Yoshiba, S., Botilde, Y., Motoyama, N., Reith, W., Durand, B., Shiratori, H., Hamada, H., 2012. Two rotating cilia in the node cavity are sufficient to break left–right symmetry in the mouse embryo. Nature communications 3, 622.

Smith, D., Blake, J., Gaffney, E., 2008. Fluid mechanics of nodal flow due to embryonic primary cilia. Journal of The Royal Society Interface 5 (22), 567–573.

Smith, D., Montenegro-Johnson, T., Lopes, S., 2019. Symmetry-breaking cilia-driven flow in embryogenesis. Annual Review of Fluid Mechanics 51, https://doi.org/10.1146/annurev–fluid–010518–040231.

Smith, D., Smith, A., Blake, J., 2011. Mathematical embryology: the fluid mechanics of nodal cilia. J. Eng. Math. 70 (1-3), 255–279.

Tanaka, Y., Okada, Y., Hirokawa, N., 2005. Fgf-induced vesicular release of sonic hedgehog and retinoic acid in leftward nodal flow is critical for left–right determination. Nature 435 (7039), 172–177.

Tavares, B., Jacinto, R., Sampaio, P., Pestana, S., Pinto, A., Vaz, A., Roxo-Rosa, M., Gardner, R., Lopes, T., Schilling, B., et al., 2017. Notch/her12 signalling modulates, motile/immotile cilia ratio downstream of foxj1a in zebrafish left-right organizer. eLife 6.